Dalton Transactions

PAPER

View Article Online
View Journal | View Issue

Cite this: *Dalton Trans.*, 2019, **48**, 15679

Comparison of two field-induced Er^{III} single ion magnets†

Irina A. Kühne, *[a,b] Liviu Ungur, [c] Kane Esien,[d] Anthony B. Carter, [e,f] John D. Gordon, [b] Cameron Pauly, [a] Helge Müller-Bunz,[a] Solveig Felton, [d] Dominic Zerulla [b] and Grace G. Morgan *[a]

Received 8th June 2019,
Accepted 3rd September 2019

DOI: 10.1039/c9dt02434d

rsc.li/dalton

We present the synthesis, magnetic and photophysical properties of four mononuclear Ln^{III} complexes in two isostructural lattices containing Gd^{III} and Er^{III}. A heptadentate Schiff base ligand and acetate *versus* trifluoroacetate were used to synthesise complexes **1–4**, among which the two Er^{III} complexes **2** and **4** exhibit field-induced SIM behaviour with almost similar U_{eff} values (31.6 K for **2** and 32.7 K for **4**). *Ab initio* calculations show the structure of the low-lying energy states and highlight that there is already significant tunnelling in the ground doublet state, but the application of a weak magnetic field of 0.05 T is sufficient for ac magnetic measurements to suppress tunnelling in the ground state. The calculated main magnetic axes (g_Z) of the ground Kramers doublets show small differences between the two Er^{III} compounds **2** and **4** due to their different ligand fields.

Introduction

Since the discovery of slow magnetic relaxation at low temperature in a Mn_{12} complex,[1] the pursuit of single molecule magnets (SMMs) has generated intense interest. The majority of reports on monometallic lanthanide SMMs, termed single ion magnets (SIMs), focus overwhelmingly on Tb^{III} and Dy^{III} (ref. 2–5) ions which have an oblate electron density distribution. This has culminated in the recent report of a record magnetic blocking temperature (80 K) in a Dy^{III} metallocene compound.[6] The design features of Tb^{III} and Dy^{III} SIMs often include strong axial ligands which maximize the magnetic anisotropy along one axis.[7] This design paradigm should be reversed for 4f-ions with prolate electron density such as Er^{III} and Tm^{III}, *i.e.* ligands with many equatorial donors should promote slow magnetic relaxation in these ions. The shape of the free Er^{III} ion is rather prolate, although not as prolate as in the case of Tm^{III} or Yb^{III}.[7] In the case of Er^{III} based SMMs it is often seen that the shape cannot be strictly defined as oblate or prolate.[8,18] Indeed, although this is a popular approach, Sessoli *et al.* have highlighted recently that the general assumption that the slow dynamics of magnetization is associated with the magnetic anisotropy in lanthanide complexes is invalid.[8] The design principles for successful SIM preparation have matured over the last five years and reports of both field-induced and natural SIMs using Er^{III} ions have appeared steadily over this period. These include sandwich complexes with pairs of COT or COT″ derivative ligands,[9–12] pairs of cp* or mixed COT/cp ligands[13,14] or pairs of phthalocyanine donors.[15,16] Tang *et al.* reported the magnetic properties of $[Er^{III}\{N(SiMe_3)_2\}_3]$, the first example of an equatorially coordinated Er-SIM.[17] Notably, the isostructural Dy^{III} analogue does not show any SIM behaviour. To some extent, this discrepancy is expected due to the equatorially coordinating crystal field, which is more favourable to the prolate Er^{III} ion than to the oblate Dy^{III} ion.[7] More recently, Dunbar *et al.* reported the first trigonal-pyramidal Er^{III} SIM, which shows slow relaxation of magnetization under zero applied dc field with an effective barrier of U_{eff} = 63.3 K.[18] Many of these highlighted compounds are, however, air-sensitive which complicates their integration into devices for practical applications.

Here we report two new Er^{III} SIMs using a heptadentate Schiff base chelating ligand and different anionic exogenous donors. The aim was to use our previous experience with designing targeted binding pockets utilising Schiff base reactions[19] to synthesise this heptadentate ligand, H_2L_1 (Scheme 1),

[a]*School of Chemistry, University College Dublin, Belfield, Dublin 4, Ireland. E-mail: Irina.kuhne@ucd.ie*
[b]*School of Physics, University College Dublin, Belfield, Dublin 4, Ireland*
[c]*Department of Chemistry, National University of Singapore, Block S8 Level 3, 3 Science Drive 3, Singapore 117543*
[d]*Centre for Nanostructured Media, School of Mathematics and Physics, Queen's University Belfast, BT7 1NN, UK*
[e]*Institute of Inorganic Chemistry, Karlsruhe Institute of Technology (KIT), Engesserstr. 15, 76131 Karlsruhe, Germany*
[f]*School of Chemistry, University of Southampton, University Road, Southampton SO17 1BJ, UK*

†Electronic supplementary information (ESI) available. CCDC 1916223–1916226. For ESI and crystallographic data in CIF or other electronic format see DOI: 10.1039/C9DT02434D

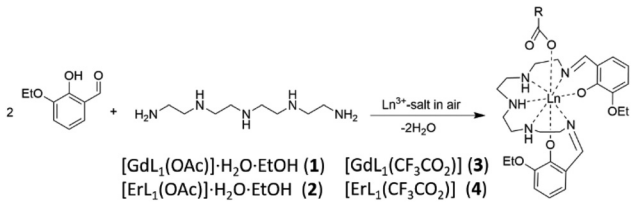

Scheme 1 General synthetic approach leading to the formation of the monomeric compounds $[LnL_1(OAc)]\cdot H_2O\cdot EtOH$ with Ln = Gd (**1**) and Er (**2**) and $[GdL_1(CF_3CO_2)]$ with Ln = Gd (**3**) and Er (**4**).

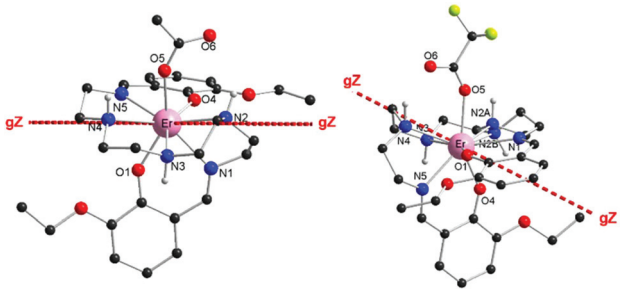

Fig. 1 Molecular structures of **2** (left) and **4** (right) (organic H atoms and solvent molecules omitted for clarity; carbon - black, nitrogen - blue, oxygen - red, fluorine - yellow, erbium - pink). The red dashed lines represent the calculated main magnetic axes (g_Z) in the ground Kramers doublets with respect to the molecular frames. For **2** (left), the g_Z axis makes an angle of 70.5° with Er-O5, 23.8° with Er-N2 and 28.9° with Er-N5. For **4**, the g_Z axis makes an angle of 69.5° with Er-O5, 61° with Er-O1, and 34.6° with Er-N1.

for its ability to form a large pocket suitable for capturing a single Ln^{III} ion. In the second step we tried to fine tune the crystal field around the Ln^{III} ion by using different types of capping ligands. The analogous Gd^{III} complexes were prepared to assess the degree of intermolecular magnetic interactions in order to show that the magnetic centres were well separated.

This approach resulted in a monomeric coordination complex, similar to the previously published Lu^{III} containing complex.[20]

The reaction using $Ln(OAc)_3$ led to the formation of monomeric structures $[LnL_1(OAc)]\cdot H_2O\cdot EtOH$ with Ln = Gd (**1**) and Er (**2**). Since the ligand field around the metal centre has an influence on the magnetic properties,[21] the electron withdrawing trifluoro group was introduced under the same reaction conditions, and monomeric structures $[GdL_1(CF_3CO_2)]$ **3**, and $[ErL_1(CF_3CO_2)]$ **4** were formed.

Results and discussion

In order to stabilise the formation of a monomeric species, we decided to introduce the bulky anionic ligands, acetate and trifluoroacetate, respectively, since the heptadentate ligand provided only two negative charges, and it was necessary to have a third negative charge to support a Ln^{3+} centre. This approach was taken because the design of molecular symmetry is the only method for controlling the magnetic behaviour of mononuclear lanthanide compounds, while ligand modification provides a second route towards improving/changing the magnetic properties. This is confirmed by recent experimental and theoretical studies of low coordinate Ln^{3+} complexes which suggest that it is not only the coordinating donor atoms and their ligand fields that determine the anisotropy of Ln SIMs but also the electrostatic potential of the entire ligand.[22]

Single crystal structural analysis reveals that complexes **1** and **2** are isostructural and crystallise in the orthorhombic space group $P2_12_12_1$ with $Z = 4$, while complexes **3** and **4** crystallise in the monoclinic space group $P2_1/c$, also with $Z = 4$. The coordination sphere in all compounds is composed of the $N_5O_2^{2-}$ donor set from the chelating ligand and the additional carboxylate oxygen (Fig. 1).

The central lanthanide ion is chelated by the dianionic heptadentate Schiff base ligand, L_1^{2-}, and the deprotonated oxygen atom, O5, of the carboxylate co-ligand, resulting in an eight-coordinated environment (Fig. 1).

All bond lengths are summarized in Table S1, ESI.† There are three Ln–O bonds in the acetate containing complexes **1** and **2**, where the bond length to the acetate oxygen O5 is 2.31 Å, which is slightly longer than the Ln–O bond lengths to the phenol oxygen atoms, O1 and O4, which are 2.22 and 2.26 Å, respectively. Complexes **2** and **4** show similar bond lengths towards O1 and O4, but their bond lengths to the deprotonated oxygen O5 are about 0.1 Å longer than in the case of complexes **1** and **2**, which is expected due to the electron withdrawing nature of trifluoroacetate. The Ln–N bond lengths range from 2.51 to 2.62 Å for **1** and **2**, which is similar for **3** and **4**. The Schiff base ligand contains two types of nitrogen donors, two imines, N1 and N5, and three amines, N2, N3 and N4. The bond lengths to the imine nitrogen atoms are, as expected, slightly shorter than those to the amines. In the case of complexes **3** and **4**, the tetraethylenepentamine backbone shows a disorder around the N2 atoms.

It is well known that the coordination geometry of lanthanide ions has an important influence on the magnetic behaviour.[3,7,23] The pentamine backbone (N1–N5) together with one phenyl ring of the ligand, O4, form an almost perfect plane around the central Ln^{III} (see Fig. 2) with only N1 and N2 being slightly above and below the plane (N4 and N5 for compounds **3** and **4**, respectively). A second plane, almost perpendicular to the first one (82° for complex **2** and 87° for complex **4**), is spanned by the second phenol ring, and the carboxylate oxygens, O5 and O6 (see Fig. 2).

Since Rinehart and Long published their article about the relationship between anisotropy and structure in 2011[7] it is known that the coordination geometry around the lanthanide ion influences the magnetic behavior. The shape of the free Er^{III} ion is rather prolate, although not as prolate as in the case of Tm^{III} or Yb^{III}.[7] In the case of Er^{III} based SMMs it is often seen that the shape cannot be strictly defined as oblate or prolate.[8,18] In order to describe the geometries of lanthanide ions within the structures, they were analysed using the software SHAPE.[24] The continuous shape measure accompany-

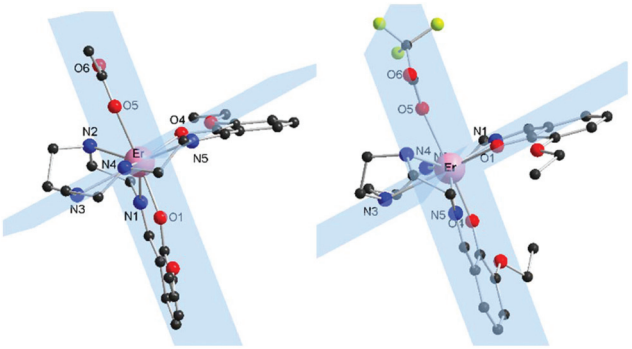

Fig. 2 Molecular structures of **2** (left) and **4** (right) forming two almost perpendicular planes around the central Ln^{III} centre, with an angle between the planes of 82° for complex **1** and 87° for complex **3**.

ing each geometry is a measure of how much it deviates from an idealized polyhedron, zero being ideal. While compounds **1** and **2** are closer to a biaugmented trigonal prismatic geometry, as shown in Fig. 3, complexes **3** and **4** show less deviation from an idealized triangular dodecahedron (see Table S2†). Due to the flexibility of the Schiff base ligand, the coordination geometry around complexes **2** and **4** is rather spherical, with compounds **1** and **2** closer to C_{2v} symmetry and **3** and **4** closer to D_{2d}.

The molecular structures of **1** and **2** contain a water molecule and an ethanol molecule, leading to an overall formula of $[LnL_1(OAc)]\cdot H_2O\cdot EtOH$, which is due to the formation of hydrogen bonds (see Fig. 4) between the hydrogen atoms of the water molecule, O8, and the neighbouring carboxylate oxygen, O6, and the oxygens of the Schiff base ligand, O3 and O4. In addition, the hydrogen atom of one of the amine groups of the ligand's backbone, N2, forms a hydrogen bond with the oxygen atom of the water molecule, as highlighted in Fig. 4. On the other hand, complexes **3** and **4** crystallize without any solvent in the crystal lattice but form strong H-bonds through the electronegative trifluoro group (see Fig. 4, right), leading to the formation of two closely neighboured monomeric units along the *c*-axis.

The dc susceptibility measurements were performed on all four compounds which were studied between 1.8 and 300 K under an applied field of 1000 Oe (Fig. 5). The room temperature $\chi_M T$ values for all complexes are in good agreement with the expected values for non-interacting Ln^{III} ions (Gd^{III}, $^8S_{7/2}$, g = 2, C = 7.88 cm^3 K mol^{-1} and Er^{III}, $^4I_{15/2}$, g = 6/5, C = 11.48 cm^3 K mol^{-1})[25] with values of 7.85 cm^3 K mol^{-1} for complex **1** (7.89 cm^3 K mol^{-1} for **3**) and 11.28 cm^3 K mol^{-1} for complex **2** (11.48 cm^3 K mol^{-1} for **4**). On lowering the temperature, the $\chi_M T$ product for the Gd^{III} containing complexes **1** and **3** remains almost constant, while that for the Er^{III} containing complexes **2** and **4** starts to decrease on cooling to reach the final minimum at 1.8 K.

Field dependence of magnetization was measured at different temperatures and the data are shown in Fig. 6 for the Gd^{III} containing complexes **1** and **3**. For both compounds, the magnetization curves measured at low temperatures show a

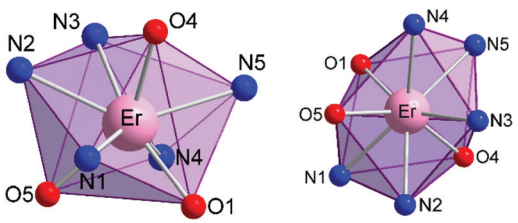

Fig. 3 SHAPE analysis showing the biaugmented trigonal prismatic environment of complex **2** (left) and the triangular dodecahedron of complex **4** (right).

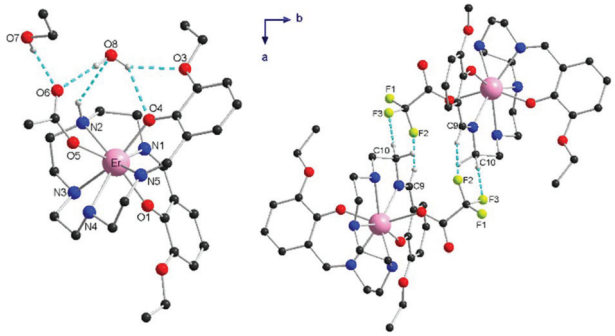

Fig. 4 Molecular structures of $[ErL_1(OAc)]\cdot H_2O\cdot EtOH$ **2** (left) and $[ErL_1(CF_3CO_2)]$ **4** (right) highlighting the formation of hydrogen bonds as turquoise dashed lines.

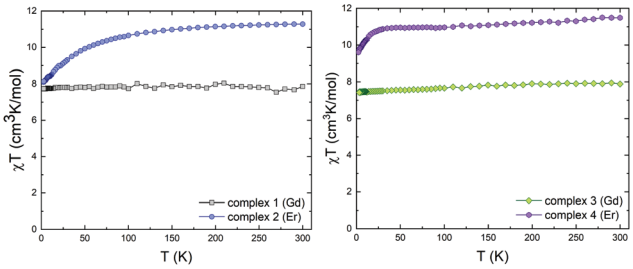

Fig. 5 Temperature dependence of the $\chi_M T$ product at 1000 Oe for complexes **1** and **2** with the acetate co-ligand (left) and for complexes **3** and **4** containing the trifluoroacetate co-ligand (right).

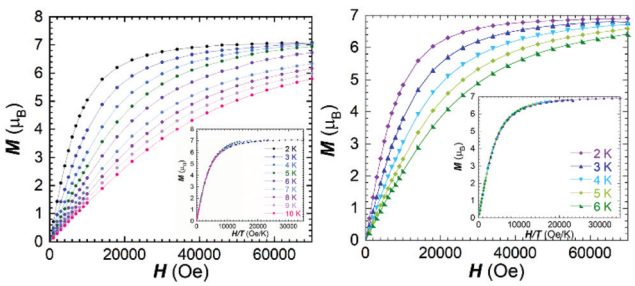

Fig. 6 Field dependence of magnetization and reduced magnetization (inset) for $[GdL_1OAc]\cdot EtOH\cdot H_2O$ **1** (left) and $[GdL_1(CF_3CO_2)]$ **3** (right) measured between 0 and 7 T at different temperatures.

clear saturation above 3 T and the reduced magnetization shows the superposition of all isotherms on one master curve, as expected for an isotropic system. The saturation values of 7.05μ_B at 7 T and 2 K for **1** and 6.95μ_B for **3**, respectively, are in good agreement with the expected 7.0μ_B for one completely uncoupled Gd^{III} (S = 7/2) ion. This demonstrates that there are no long-range interactions which is important when investigating the magnetic response of an anisotropic Er^{III} compound.

The field dependence of magnetization for both Er^{III} containing compounds, **2** and **4**, were measured at 2, 3 and 5 K and are shown in Fig. S1 and S2.† In both cases, the magnetization curves do not saturate at high fields which indicates the presence of significant magnetic anisotropy and/or low-lying excited states. The values of the isotherms rapidly increase at low fields before following a more gradual linear increase after 1.5 T, without saturation, reaching a value of 5.2μ_B at 7.0 T in both complexes. The anisotropy present in both compounds can be seen from the reduced magnetization plots shown as M *vs.* H/T (see Fig. S1 and S2†) which clearly do not superimpose on to a single master curve.

In order to investigate the potential presence of slow relaxation of magnetization caused from SMM behaviour, ac magnetic susceptibility measurements were performed on both Er^{III} containing complexes **2** and **4**. In attempts to suppress any quantum tunnelling of magnetization (QTM), the frequency-dependent ac susceptibility was measured at dc fields ranging from 0 to 3000 Oe (Fig. S3 and S4†), which in both cases showed the field-dependent in-phase and out-of-phase ac susceptibility signals, and the optimum field was found to be 500 Oe. For both Er^{III} complexes **2** and **4**, ac measurements were carried out under this optimum external dc field of 500 Oe and the obtained in-phase and out-of-phase susceptibility signals are shown in Fig. 7.

In both cases, the ac measurements revealed the temperature dependent in-phase and out-of-phase signals over the whole applied temperature range with clear maxima up to 3.5 K. The maxima of the frequency dependent out-of-phase susceptibility curves were used to extract the relaxation time as a function of temperature and were plotted as ln(τ) *versus* 1/T (see Fig. S5†). In the case of [ErL_1OAc]·EtOH·H_2O **2**, the temperature dependent in-phase and out-of-phase susceptibility were also measured at different frequencies (see Fig. S6†) in order to check for secondary relaxation processes at higher temperatures, which were found to be absent.

Cole–Cole plots of χ'_M *versus* χ''_M between 1.8 and 4.0 K (Fig. S7†) have semicircular profiles, indicating a single relaxation process and were fitted with CC-Fit,[26] which uses a generalized Debye model.[27] The obtained α-values range between 0.1 (2.2 K) and 0.02 (4.0 K) for complex **2** and between 0.08 (1.8 K) and 0.04 (3.5 K) for complex **4**, indicating a narrow relaxation time distribution. The extracted parameters (see Tables S3 and S4, ESI†) were plotted as ln(τ) *versus* 1/T (see Fig. S5, ESI†), leading to a linear fit curve, resembling the Arrhenius equation giving U_{eff} = 31.6 K and $\tau_0 = 2.6 \times 10^{-8}$ s (R = 0.99) for complex **2**. The Arrhenius fit for complex **4** shows

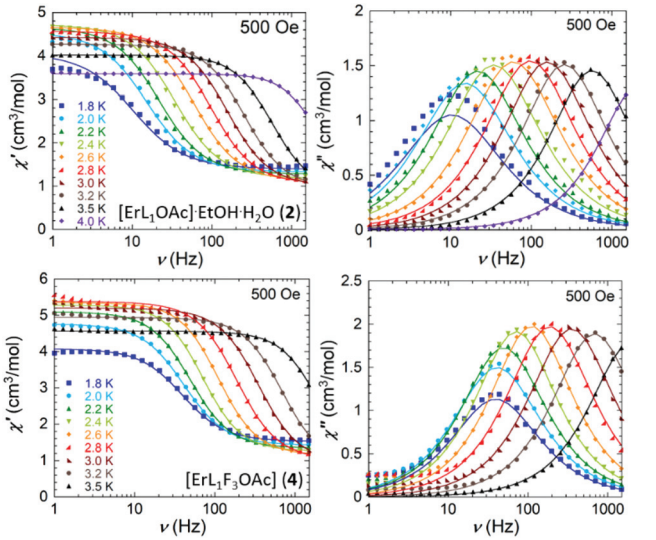

Fig. 7 Frequency-dependence of the in-phase (left) and out-of-phase susceptibility (right) at 500 Oe of [ErL_1OAc]·EtOH·H_2O **2** (top) and [$ErL_1CF3CO2$] **4** (bottom) in a temperature range between 1.8 and 4.0 K (the solid line represents the best fit obtained using CC-Fit which uses a generalized Debye model).

a slight increase in the energy barrier, U_{eff} = 32.7 K and deceleration of the relaxation time to $\tau_0 = 7.7 \times 10^{-9}$ s (R = 0.99) in comparison to complex **2**. In the case of complex **4**, the Cole–Cole plots revealed the start of a second process at small frequencies and at temperatures above 2.8 K. Therefore, ac measurements were carried out under an external dc field of 1500 Oe for complex **4** to investigate the dynamic magnetic processes and the in-phase and out-of-phase susceptibility signals (Fig. S8, ESI†). The Cole–Cole plots at 1500 Oe of χ'_M *versus* χ''_M between 1.8 and 3.0 K (Fig. S9, ESI†) clearly show the beginning of the second process over the full temperature range and the plots were fitted to the sum of two modified Debye functions, but the resulting parameters did not lead to satisfying results which indicates that there is probably more than one relaxation process taking place.

The Er^{III} ion in the first Er^{III} SIM, the [ErDOTA] complex, from Sessoli *et al.*[28] exhibits a quite regular square antiprismatic geometry and shows the anticipated frequency-dependence in the out-of-phase susceptibility, resulting in an U_{eff} of 39 K.[28] Due to the flexibility of the heptadentate ligand, the symmetry around the Ln^{III} centres within compounds **1–4** is quite low. While complex **2** exhibits a biaugmented trigonal prismatic geometry, complex **4** is closer to have a triangular dodecahedral environment. Both have shown to exhibit similar energy barriers.

Ab initio calculations using CASSCF/RASSI and CASPT2/RASSI were performed in order to get additional insights into the low-lying energy structure and magnetic properties of the investigated compounds. Such calculations have been previously shown to be efficient for Er^{III} compounds.[29–31] The calculated energy spectra for complexes **2** and **4** are shown in Fig. 8, where the states are plotted as a function of the intrin-

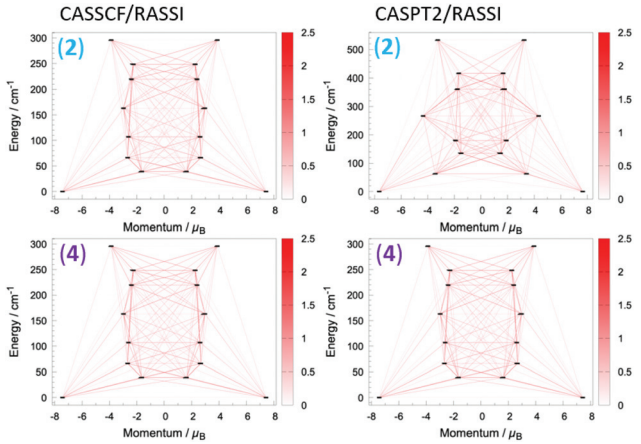

Fig. 8 Energy diagram for the blocking barrier for complex **2** (top) and **4** (bottom) using the VDZP basis set. Energy spectrum and the blocking barrier of **2** (top) and **4** (bottom). Each doublet state $\pm M_J$ arising from a given atomic multiplet is placed according to its magnetic moment (horizontal axis). The intensity of the red lines indicates the amplitude of the average transition magnetic dipole moment in Bohr magneton between the connected states (see the legend on the left of each plot), the square of which roughly scales with the rate of spin-phonon transition between them.[32,33] The most intense lines outline the magnetization blocking barrier (shown as red lines).

sic magnetic moment. Each doublet state $\pm M_J$ arising from a given atomic multiplet is placed according to its magnetic moment (horizontal axis). The intensity of the red lines indicates the amplitude of the average transition magnetic dipole moment in Bohr magnetons between the connected states (see the legend on the left of each plot), the square of which roughly scales with the rate of spin-phonon transition between them.[32,33] The red lines connecting the states are average values of the transition magnetic moment connecting the states. The magnetization blocking barrier is understood as the path connecting the most intense lines. Table 1 gives the numerical values of the calculated energy spectra in several computational approximations and the *g*-tensors of the low-lying Kramers doublets. The orientation of the ground state g_Z main magnetic axes of **2** and **4** with respect to their molecular frames are shown in Fig. 1, using the calculated results. It is clear that $g_{X,Y}$ values are, on average, larger for **4** compared to **2**, for all computational models employed. This is in line with the fact that the peaks in χ''_M appear at larger frequencies for **4** (see Fig. 7), which is a direct sign of the higher speed of magnetic relaxation of **4** compared to **2**.

The data in Fig. 8 and Table 1 show that there is already significant tunnelling in the ground doublet state (reflected in the large values of g_x and g_y). The temperature assisted tunnelling in the first and higher excited doublet states for **2** and **4** is also significant (Fig. 8). This means that even if a weak magnetic field applied for ac magnetic measurements (Fig. 7) may suppress tunnelling in the ground state, it is not sufficient to prevent relaxation *via* the excited states and other mechanisms.

Table 1 Energy spectra (cm^{-1}) of the investigated compounds and the main values of the g tensors of the ground Kramers doublet in various computational approximations

$[ErL_1(OAc)]\cdot H_2O\cdot EtOH$ (**2**)			$[ErL_1(CF_3CO_2)]$ (**4**)		
VDZP, CASSCF	VTZP, CASSCF	VDZP, CASPT2	VDZP, CASSCF	VTZP, CASSCF	VDZP, CASPT2
0	0	0	0	0	0
42	41	63	39	39	58
89	91	135	66	71	102
118	122	180	107	110	161
173	175	266	163	163	251
236	239	361	219	227	337
273	277	416	248	259	383
353	367	533	296	301	454
Main values of the **g** tensor in the ground Kramers doublet					
0.212	0.231	0.180	0.183	0.161	0.306
0.830	0.883	0.720	1.158	1.326	1.599
15.413	15.317	15.301	14.867	15.000	14.664

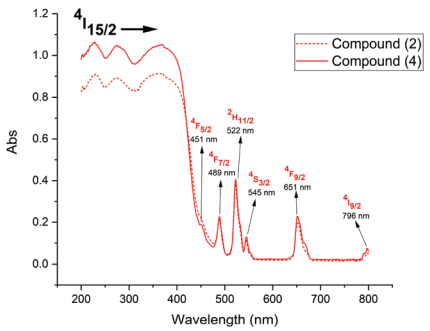

Fig. 9 Electronic absorption spectra of powdered samples of the Er^{III} containing complexes **2** and **4** in the visible range (200–800 nm) at 293 K. Spectra were recorded in diffuse reflectance mode.

Diffuse spectral reflectance measurements of the ground crystalline powders of the two Gd^{III} containing complexes **1** and **3** show the characteristic triple peaks associated with *o*-vanillin based complexes (see Fig. S10†). However, they have been shifted to a lower energy with the peaks here reported at 363 nm, 280 nm, and 232 nm compared with 348 nm, 266 nm, and 220 nm, respectively. When examining the Er^{III} containing complexes **2** and **4**, shown in Fig. 9, the sharp peaks characteristic of the erbium transitions were observed. These are assigned as $^4I_{15/2}$ to $^4F_{5/2}$, $^4F_{7/2}$, $^2H_{11/2}$, $^4S_{3/2}$, $^4F_{9/2}$, and $^4I_{9/2}$ based on previously reported solid state samples.[34,35]

Conclusions

We have presented the synthesis, structural and magnetic properties of a family of two almost isostructural Er^{III} compounds. The heptadentate ligand and the acetate derivative lead to the formation of mononuclear species which show field-induced SIM behaviour with almost similar U_{eff} values (31.6 K for **2** and 32.7 K for **4**). The rather flexible heptadentate Schiff base ligand is responsible for the low symmetry around

the Ln^{III} centres and while complexes **1** and **2** exhibit a biaugmented trigonal prismatic geometry, compounds **3** and **4** are closer to have a triangular dodecahedral environment. *Ab initio* calculations highlight the low-lying energy spectra. The calculated values of the *g*-tensors of the low-lying Kramers doublets show one preferred direction, g_z, as the easy axis of the molecule. While $g_{X,Y}$ values are, on average, larger for **4** in comparison to complex **2**, this is in agreement with the higher speed of magnetic relaxation of **4** compared to **2**.

The magnetic data and the calculations are in good agreement and show that there is already significant tunnelling in the ground doublet state which is reflected in the large values of g_x and g_y. Both compounds **2** and **4** exhibit significant temperature assisted tunnelling in the first and higher excited doublet states, but the application of a weak magnetic field of 0.05 T for ac magnetic measurements can suppress tunnelling in the ground state. At the same time, though, this field is not sufficient to prevent relaxation *via* the excited states and other mechanisms.

Although the Schiff base ligand has not promoted the desired high symmetry around the Ln^{III} centre, it still leads to field-induced slow relaxation of magnetization and the calculated main magnetic axes (g_Z) in the ground Kramers doublets with respect to the molecular frames show the desired outcome.

This work presents a new route towards air-stable Er^{III} SIMs which have the possibility of fine-tuning, especially of the ligand, in future applications.

Experimental

General experimental

Physical measurements. All measurements were carried out on powdered samples of the respective polycrystalline compound. Elemental analysis (C, H, and N) was performed using a PerkinElmer Vario EL. A Bruker Alpha PlatinumATIR spectrometer was used to record infrared spectra, and mass spectra were recorded on a Waters 2695 Separations Module Electrospray Spectrometer. Solid state Raman spectra were recorded at a 532 nm excitation using a specifically tailored low-frequency configuration setup.[36] In this configuration, an ASE filter to filter spontaneous emission and an ONDAX XLF to eliminate Rayleigh scattering were used with a HoloSpec f/1.8 monochromator for imaging the spectra on a cooled Andor Newton EMCCD.[37]

Magnetic measurements. The magnetic susceptibility measurements were performed using a Quantum Design SQUID magnetometer MPMS-XL operating between 1.8 and 300 K. DC measurements were performed on a polycrystalline sample of 14.5 mg of $[GdL_1OAc]$ **1**, 26.0 mg of $[ErL_1OAc]$ **2**, 9.8 mg of $[GdL_1(CF_3CO_2)]$ **3** and 12.8 mg of $[ErL_1(CF_3CO_2)]$ **4**. Each sample was wrapped in a polyethylene membrane and subjected to fields in the range from 0 to 7 T. The magnetization data were obtained at 100 K in order to check for ferromagnetic impurities, which were found to be absent in the samples. Diamagnetic corrections were applied to correct for contribution from a sample holder, and the inherent diamagnetism of the sample was estimated using Pascal's constants. AC measurements were carried out at frequencies between 1 and 1500 Hz.

UV-vis collection details. Solid state diffuse spectral reflectance measurements were carried out on lightly ground crystalline samples of complexes **1–4** pressed onto a flat barium oxide surface against a barium oxide standard. The spectra were recorded using a Shimadzu UV-2700 spectrophotometer equipped with an ISR-2600 integrating sphere attachment.

Materials and synthetic procedures

Starting materials. All chemicals and solvents if not otherwise mentioned were purchased from chemical companies and were of reagent grade. They were used without any further purification or drying. All reactions were carried out under ambient conditions. All measurements were carried out on powdered samples of the respective polycrystalline compound. The $Ln(OAc)_3{\cdot}6H_2O$ and $Gd(CF_3CO_2)_3{\cdot}xH_2O$ salts were prepared from Ln_2O_3 with respective acids, according to the literature.

Synthesis and characterization of complexes 1–4

1: $[Gd(L_1)(OAc)]{\cdot}EtOH{\cdot}H_2O$: Tetraethylenepentamine (0.25 mmol, 47 mg) was dissolved in a 1 : 1 mixture of EtOH/MeCN (20 ml). 3-Ethoxysalicylaldehyde (0.5 mmol, 83 mg) was added to the solution, resulting in an immediate colour change to bright yellow. The ligand solution was stirred for one hour under ambient conditions to complete the Schiff base reaction and was then used directly without any further purification.

Solid $Gd(OAc)_3{\cdot}xH_2O$ (0.25 mmol, 96 mg) was then added to the ligand solution and the pale-yellow solution was stirred for one hour at room temperature, before being left to stand for crystallization without filtration. After one week complex **1** crystallized as pale-yellow blocks suitable for single crystal X-ray analysis.

Elemental analysis for $[Gd(L_1)(OAc)]{\cdot}EtOH{\cdot}H_2O$ ($C_{30}H_{48}GdN_5O_8$) (%): calculated: C: 47.16; H: 6.33; N: 9.17; found: C: 47.02; H: 6.10; N: 8.94.

IR (KBr): $\tilde{\nu}/cm^{-1}$ = 3540 (w) O–H; 1570 (s), 1417 (s) C–O from the acetate; 3253 (w), 1466 (s) amine N–H; 1626 (s) imine C=N; 1389 phenol (see Fig. S11†).

2–4: The complexes were synthesized following the procedure for complex **1**, using the required lanthanide acetate, or lanthanide trifluoroacetate, respectively.

2: Elemental analysis for $[Er(L_1)(CH_3CO_2)]{\cdot}EtOH{\cdot}H_2O$ ($C_{30}H_{48}ErN_5O_8$) (%): calculated: C: 46.55; H: 6.25; N: 9.05; found: C: 46.42; H: 5.99; N: 8.97.

IR spectrum is shown in Fig. S12 and S13.†

3: Elemental analysis for $C_{28}H_{37}N_5O_6GdF_3$ (%): calculated: C: 44.61; H: 4.95; N: 9.29; found: C: 44.49; H: 4.73; N: 9.16.

IR spectrum is shown in Fig. S14 and S15.†

4: Elemental analysis for $C_{28}H_{37}N_5O_6ErF_3$ (%): calculated: C: 44.03; H: 4.88; N: 9.17; F: 7.46; found: C: 43.83; H: 4.78; N: 8.95; F: 7.76.

IR spectrum is shown in Fig. S16 and S17.†

The solid-state Raman spectra of complexes **2** and **4** are shown in Fig. S18.†

Crystallography

Crystal data collection and refinement. Suitable single crystals of complexes **1–4** were mounted on Oxford Diffraction Supernova A diffractometer fitted with an Atlas detector; datasets were measured using a monochromatic Cu-Kα radiation source (complex **3** (Gd-F_3)) or a Mo-Kα radiation source (complex **1** (Gd-OAc), **2** (Er-OAc) and **4** (Er-F_3)) and corrected for absorption.[38] The temperature (100 K) was controlled with an Oxford Cryosystem instrument. Structures were solved by charge-flipping methods (SHELXT)[39] and refined with full-matrix least-squared procedures based on F^2, using SHELXL-2016. Non-hydrogen atoms were refined with independent anisotropic displacement parameters. All hydrogen atoms, including OH ones, were added at calculated positions. Selected crystallographic data and structure refinements are summarized in Table S6† and crystallographic data for the structures reported in this paper have been deposited with the Cambridge Crystallographic Data Centre as supplementary publication numbers CCDC 1916223: **1**, 1916225: **2**, 1916224: **3** and 1916226: **4**.†

Computational details

The X-ray molecular structure corresponding to the CCDC number for compounds **2** and **4** were employed for theoretical calculations. *Ab initio* calculations of RASSCF/RASPT2/RASSI/SINGLE_ANISO level were carried out within the MOLCAS package.[40,41] In this computational approach, relativistic corrections were included *via* the Douglas–Kroll–Hess formalism in two steps.[42–47] In the first step, scalar corrections were included in the basis sets used for the expansion of the molecular orbitals of the corresponding eigenstates at the multiconfigurational self-consistent field level of theory (RASSCF). To this end, we have employed the atomic natural orbital with relativistic core corrections (ANO-RCC) basis sets for this study.[48,49] Spin–orbit coupling was included in the second step (RASSI), using the obtained RASSCF states as input.[45,50] In this approach, spin–orbit interaction is described by an effective mean-field operator (AMFI).[57] Dynamical electron correlation was considered within multiconfigurational second-order perturbation theory (RASPT2).[40,47,51–54] All anisotropic magnetic properties (EPR *g*-tensors, magnetic susceptibility, molar magnetization, parameters of the effective crystal field for the ground *J*-multiplet) were computed using the SINGLE_ANISO module.[55,56]

Conflicts of interest

There are no conflicts to declare.

Acknowledgements

I. A. K. thanks the Irish Research Council (IRC) for the GOIPD/2016/503 fellowship. GGM thanks Science Foundation Ireland for generous support from Investigator Project Award 12/IP/1703. This work was supported by the CA COST Action CA15107 - MultiComp (Multi-Functional Nano-Carbon Composite Materials Network) (I. A. K., A. B. C.). I. A. K. thanks Dr. Chris Anson for his input about the structures. The scientific grants R-143-000-A80-114 and R-143-000-A65-133 from the National University of Singapore are gratefully acknowledged. Computational resources from NSCC (ASPIRE-1, grant 11001278) were used for this study. S. F. and K. E. thank the Northern Ireland Department for Economy through the US-Ireland Centre-to-Centre grant no. USI 108. A. B. C. would like to thank the EPSRC for funding through grant reference EP/M508147/1.

Notes and references

1 R. Sessoli, H. L. Tsai, A. R. Schake, S. Wang, J. B. Vincent, K. Folting, D. Gatteschi, G. Christou and D. N. Hendrickson, *J. Am. Chem. Soc.*, 1993, **115**, 1804–1816.
2 P. Zhang, Y.-N. Guo and J. Tang, *Coord. Chem. Rev.*, 2013, **257**, 1728–1763.
3 H. L. C. Feltham and S. Brooker, *Coord. Chem. Rev.*, 2014, **276**, 1–33.
4 S. G. McAdams, A.-M. Ariciu, A. K. Kostopoulos, J. P. S. Walsh and F. Tuna, *Coord. Chem. Rev.*, 2017, **346**, 216–239.
5 J.-L. Liu, Y.-C. Chen and M.-L. Tong, *Chem. Soc. Rev.*, 2018, **47**, 2431–2453.
6 F.-S. Guo, B. M. Day, Y.-C. Chen, M.-L. Tong, A. Mansikkamäki and R. A. Layfield, *Science*, 2018, **362**, 1400–1403.
7 J. D. Rinehart and J. R. Long, *Chem. Sci.*, 2011, **2**, 2078.
8 E. Lucaccini, L. Sorace, M. Perfetti, J.-P. Costes and R. Sessoli, *Chem. Commun.*, 2014, **50**, 1648–1651.
9 S.-D. Jiang, S.-S. Liu, L.-N. Zhou, B.-W. Wang, Z.-M. Wang and S. Gao, *Inorg. Chem.*, 2012, **51**, 3079–3087.
10 K. R. Meihaus and J. R. Long, *J. Am. Chem. Soc.*, 2013, **135**, 17952–17957.
11 J. J. Le Roy, I. Korobkov and M. Murugesu, *Chem. Commun.*, 2014, **50**, 1602–1604.
12 L. Ungur, J. J. Le Roy, I. Korobkov, M. Murugesu and L. F. Chibotaru, *Angew. Chem., Int. Ed.*, 2014, **53**, 4413–4417.
13 S.-D. Jiang, B.-W. Wang, H.-L. Sun, Z.-M. Wang and S. Gao, *J. Am. Chem. Soc.*, 2011, **133**, 4730–4733.
14 W. J. Evans, M. A. Johnston, R. D. Clark and J. W. Ziller, *J. Chem. Soc., Dalton Trans.*, 2000, 1609–1612.
15 R. Marx, F. Moro, M. Dörfel, L. Ungur, M. Waters, S. D. Jiang, M. Orlita, J. Taylor, W. Frey, L. F. Chibotaru and J. van Slageren, *Chem. Sci.*, 2014, **5**, 3287.

16 J. D. Hilgar, M. G. Bernbeck and J. D. Rinehart, *J. Am. Chem. Soc.*, 2019, **141**, 1913–1917.
17 P. Zhang, L. Zhang, C. Wang, S. Xue, S.-Y. Lin and J. Tang, *J. Am. Chem. Soc.*, 2014, **136**, 4484–4487.
18 A. J. Brown, D. Pinkowicz, M. R. Saber and K. R. Dunbar, *Angew. Chem., Int. Ed.*, 2015, **54**, 5864–5868.
19 S. Sundaresan, I. Kühne, C. Kelly, A. Barker, D. Salley, H. Müller-Bunz, A. Powell and G. Morgan, *Crystals*, 2018, **9**, 19.
20 P. P. K. Claire, C. J. Jones, K. W. Chiu, J. R. Thornback and M. McPartlin, *Polyhedron*, 1992, **11**, 499–500.
21 A. Upadhyay, K. R. Vignesh, C. Das, S. K. Singh, G. Rajaraman and M. Shanmugam, *Inorg. Chem.*, 2017, **56**, 14260–14276.
22 P. Zhang, J. Jung, L. Zhang, J. Tang and B. Le Guennic, *Inorg. Chem.*, 2016, **55**, 1905–1911.
23 L. Sorace, C. Benelli and D. Gatteschi, *Chem. Soc. Rev.*, 2011, **40**, 3092.
24 M. Llunell, D. Casanova, J. Cirera, P. Alemany and S. Alvarez, *SHAPE: Program for the Stereochemical Analysis of Molecular Fragments by Means of Continuous Shape Measures and Associated Tools, Version 2.1*, Barcelona, 2013.
25 C. Benelli and D. Gatteschi, *Chem. Rev.*, 2002, **102**, 2369–2388.
26 N. F. Chilton, http://www.nfchilton.com/cc-fit.html, 2014.
27 Y.-N. Guo, G.-F. Xu, Y. Guo and J. Tang, *Dalton Trans.*, 2011, **40**, 9953.
28 M.-E. Boulon, G. Cucinotta, J. Luzon, C. Degl'Innocenti, M. Perfetti, K. Bernot, G. Calvez, A. Caneschi and R. Sessoli, *Angew. Chem., Int. Ed.*, 2013, **52**, 350–354.
29 P. P. Hallmen, G. Rauhut, H. Stoll, A. O. Mitrushchenkov and J. van Slageren, *J. Chem. Theory Comput.*, 2018, **14**, 3998–4009.
30 Y. Rechkemmer, J. E. Fischer, R. Marx, M. Dörfel, P. Neugebauer, S. Horvath, M. Gysler, T. Brock-Nannestad, W. Frey, M. F. Reid and J. van Slageren, *J. Am. Chem. Soc.*, 2015, **137**, 13114–13120.
31 P. P. Hallmen, C. Köppl, G. Rauhut, H. Stoll and J. van Slageren, *J. Chem. Phys.*, 2017, **147**, 164101.
32 L. Ungur and L. F. Chibotaru, *Phys. Chem. Chem. Phys.*, 2011, **13**, 20086–20090.
33 L. Ungur, M. Thewissen, J. P. Costes, W. Wernsdorfer and L. F. Chibotaru, *Inorg. Chem.*, 2013, **52**, 6328–6337.
34 V. Naresh and S. Buddhudu, *Phys. Chem. Glasses: Eur. J. Glass Sci. Technol., Part B*, 2015, **56**, 255–262.
35 W. T. Carnall, P. R. Fields and K. Rajnak, *J. Chem. Phys.*, 1968, **49**, 4424–4442.
36 C. de Fréin, E. Lestini, N. Quirke and D. Zerulla, *Phys. Status Solidi*, 2013, **250**, 2635–2638.
37 Y. Shen, N. Quirke and D. Zerulla, *Appl. Phys. Lett.*, 2015, **106**, 201902.
38 R. C. Clark and J. S. Reid, *Acta Crystallogr., Sect. A: Found. Crystallogr.*, 1995, **51**, 887–897.
39 G. M. Sheldrick, *Acta Crystallogr., Sect. C: Struct. Chem.*, 2015, **71**, 3–8.
40 F. Aquilante, J. Autschbach, R. K. Carlson, L. F. Chibotaru, M. G. Delcey, L. De Vico, I. F. Galvan, N. Ferre, L. M. Frutos, L. Gagliardi, M. Garavelli, A. Giussani, C. E. Hoyer, G. Li Manni, H. Lischka, D. X. Ma, P. A. Malmqvist, T. Muller, A. Nenov, M. Olivucci, T. B. Pedersen, D. L. Peng, F. Plasser, B. Pritchard, M. Reiher, I. Rivalta, I. Schapiro, J. Segarra-Marti, M. Stenrup, D. G. Truhlar, L. Ungur, A. Valentini, S. Vancoillie, V. Veryazov, V. P. Vysotskiy, O. Weingart, F. Zapata and R. Lindh, *J. Comput. Chem.*, 2016, **37**, 506–541.
41 L. F. Chibotaru and L. Ungur, *J. Chem. Phys.*, 2012, **137**, 064112.
42 M. Douglas and N. M. Kroll, *Ann. Phys.*, 1974, **82**, 89–155.
43 B. A. Hess, *Phys. Rev. A*, 1986, **33**, 3742–3748.
44 M. Reiher, *Wiley Interdiscip. Rev.: Comput. Mol. Sci.*, 2012, **2**, 139–149.
45 P. A. Malmqvist, B. O. Roos and B. Schimmelpfennig, *Chem. Phys. Lett.*, 2002, **357**, 230–240.
46 J. Paulovic, T. Nakajima, K. Hirao, R. Lindh and P. A. Malmqvist, *J. Chem. Phys.*, 2003, **119**, 798–805.
47 B. O. Roos and P. A. Malmqvist, *Phys. Chem. Chem. Phys.*, 2004, **6**, 2919–2927.
48 B. O. Roos, R. Lindh, P. A. Malmqvist, V. Veryazov, P. O. Widmark and A. C. Borin, *J. Phys. Chem. A*, 2008, **112**, 11431–11435.
49 B. O. Roos, R. Lindh, P. A. Malmqvist, V. Veryazov and P. O. Widmark, *J. Phys. Chem. A*, 2004, **108**, 2851–2858.
50 P. A. Malmqvist and B. O. Roos, *Chem. Phys. Lett.*, 1989, **155**, 189–194.
51 B. O. Roos, K. Andersson, M. P. Fulscher, P. A. Malmqvist, L. SerranoAndres, K. Pierloot and M. Merchan, *Adv. Chem. Phys.*, 1996, **93**, 219–331.
52 J. Finley, P.-Å. Malmqvist, B. O. Roos and L. Serrano-Andrés, *Chem. Phys. Lett.*, 1998, **288**, 299.
53 G. Ghigo, B. O. Roos and P. A. Malmqvist, *Chem. Phys. Lett.*, 2004, **396**, 142–149.
54 S. Vancoillie, M. G. Delcey, R. Lindh, V. Vysotskiy, P. A. Malmqvist and V. Veryazov, *J. Comput. Chem.*, 2013, **34**, 1937–1948.
55 L. Ungur and L. F. Chibotaru, *Chem. – Eur. J.*, 2017, **23**, 3708–3718.
56 L. F. Chibotaru and L. Ungur, *J. Chem. Phys.*, 2012, **137**, 22.
57 B. A. Hess, C. M. Marian, U. Wahlgren and O. Gropen, *Chem. Phys. Lett.*, 1996, **251**, 365–371.